Surface & Coatings Technology 454 (2023) 129188

Contents lists available at ScienceDirect

Surface & Coatings Technology

journal homepage: www.elsevier.com/locate/surfcoat

Microwave plasma-assisted reactive HiPIMS of InN films: Plasma environment and material characterisation

Caroline Hain [a,b,c,*], Peter Schweizer [c], Patrick Sturm [d], Aurelio Borzì [e], Jonathan E. Thomet [b], Johann Michler [c], Aïcha Hessler-Wyser [b], Thomas Nelis [a,c]

[a] Institute for Applied Laser, Photonics and Surface Technologies, BFH, Bern University of Applied Sciences, Quellgasse 21, 2502 Biel/Bienne, Switzerland
[b] Laboratory for Photovoltaics and Thin Film Electronics, EPFL, École Polytechnique Fédérale de Lausanne, Rue de la Maladière 71b, 2000 Neuchâtel, Switzerland
[c] Laboratory for Mechanics of Materials and Nanostructures, Empa, Swiss Federal Laboratories for Materials Science and Technology, Feuerwerkerstrasse 39, 3602 Thun, Switzerland
[d] TOFWERK AG, Schorenstrasse 39, 3645 Thun, Switzerland
[e] Center for X-ray Analytics, Empa, Swiss Federal Laboratories for Materials Science and Technology, Überlandstrasse 129, 8600 Dübendorf, Switzerland

ARTICLE INFO

Keywords:
Microwave plasma
Reactive HiPIMS
Indium7 nitride
Plasma characterisation
ToF-MS

ABSTRACT

This work focuses on the low temperature fabrication process of InN thin films via microwave plasma-assisted reactive high power impulse magnetron sputtering (MAR-HiPIMS). The influence of microwave plasma on the HiPIMS discharge process at various nitrogen flows and microwave powers was monitored and characterised through in situ diagnostics, including following HiPIMS I(*V*,*t*) curves, optical emission spectroscopy (OES), as well as performing time-resolved Langmuir probe and time-of-flight mass spectroscopy (ToF-MS) measurements. This was followed by the deposition of InN films via standard reactive HiPIMS (reference sample) and MAR-HiPIMS and their characterisation via X-ray diffraction (XRD), reflectometry (XRR), as well as scanning and transmission electron microscopy (SEM, TEM). It was found that the microwave plasma facilitates the dissociation/activation of nitrogen species and supplies seed electrons to the magnetron discharge plasma. Furthermore, the energy of the incoming ions was determined via ToF-MS, and it was possible to identify their plasma origin and temporal behaviour. The produced R-HiPIMS sample was highly metallic, with no nitride phase detected. The MAR-HiPMS film, however, was stoichiometric and exhibited (0002) direction texturing, with an optical bandgap of approx. 1.5 eV, electron concentration of 2.72×10^{20} cm^{-3} and electron mobility of 7.16 cm^{2}V^{-1} s^{-1} (in the range for polycrystalline InN).

1. Introduction

Reactive magnetron sputtering is a deposition technique combining aspects of both physical and chemical vapour deposition, through which compound films are produced by sputtering from a non-compound target in the presence of reactive gases, e.g. oxygen or nitrogen [1,2]. This process is advantageous over compound target sputtering, as compound targets of the desired stoichiometry and purity are often difficult to produce, resulting in non-stoichiometric films. Furthermore, they are usually non-conductive and limited to radiofrequency (RF) sputtering. However, when adding a reactive gas to the inert working gas, chemical reactions can occur on the target's surface to induce so-called target poisoning, where a compound layer forms [3]. With this, the discharge behaviour of the target can change significantly, most notably due to differences in the secondary electron emission coefficient (γ_{see}). The extent of the change depends on both the target material and type of reactive gas, as studied by Depla et al. [4]. In some cases, e.g. indium upon nitriding, the γ_{see} considerably decreases. With the electron population being a key parameter in igniting and sustaining magnetron discharges, a drop in γ_{see} can disrupt the sputtering process. In the case of reactive high power impulse magnetron sputtering (R-HiPIMS), this can result in the generation of time lags, i.e. delays in current onset [5], despite the use of high voltages during discharge ignition. Such difficulties will, in turn, cause problems in film fabrication process control and reproducibility.

Another aspect of reactive sputtering is ensuring compound material

* Corresponding author at: Institute for Applied Laser, Photonics and Surface Technologies, BFH, Bern University of Applied Sciences, Quellgasse 21, 2502 Biel/Bienne, Switzerland.
E-mail address: caroline.hain@bfh.ch (C. Hain).

https://doi.org/10.1016/j.surfcoat.2022.129188
Received 15 August 2022; Received in revised form 14 December 2022; Accepted 19 December 2022
Available online 23 December 2022

deposition of the desired stoichiometry, structure and applicational properties. This can be greatly influenced by reactions occurring between the sputtered material and reactive gas. Nitrogen is rather inert, therefore, to ensure its dissociation and reactive species generation, different strategies have been tested, ranging from applying direct current (DC) and RF, to the incorporation of additional ionisation sources [6–9]. In particular, electron cyclotron resonance (ECR) [10–13] has been reported to improve reactive gas dissociation and film property optimisation for both oxides and nitrides.

Despite various reported studies on reactive sputtering, there are still aspects that have not been investigated in detail. These include studying the influence of reactive gas on the deposition environment and determining the means to provide enough reactive species to obtain stoichiometric compound materials. Therefore, in this work, the plasma conditions during indium nitride (InN) thin film fabrication via microwave plasma-assisted reactive HiPIMS (MAR-HiPIMS) were studied.

InN is a III-V semiconductor with a variable bandgap [14–17], and high electron mobility [18], due to which it is used for various applications in optoelectronics. It is among the more difficult nitrides to produce, owing to its low dissociation temperature (500 °C), causing InN decomposition into metallic In and N_2 gas [19–21]. Reactive sputtering enables depositing materials usually at much lower temperatures than its chemical-based counterparts, however, stoichiometric InN fabrication can still be challenging. Natarajan et al. stated that only atomic nitrogen chemisorbs on pure indium [6], however, in view of the complexity of interactions between activated nitrogen, i.e. metastable and ionic N_2, and metallic surfaces [22], it is unlikely that only atomic nitrogen participates in the formation of InN. Nevertheless, as ground state N_2 does not react with indium, efficient nitrogen activation is beneficial for InN growth. Therefore, combining low temperature reactive sputtering with additional means to create reactive nitrogen species within a volume microwave plasma could prove beneficial for InN film fabrication. This is particularly true in view of competing oxidation reactions with residual oxygen present in the discharge chamber, as it can deteriorate InN's applicational properties [23].

With that in mind, besides in situ deposition environment analyses, the structure and optoelectronic properties of the obtained InN thin films were studied.

2. Experimental section

2.1. Deposition setup

The used deposition chamber was a HEXL Modular Deposition System, equipped with one magnetron in unbalanced configuration (Korvus Technology). The chamber was evacuated using HiPace 700 molecular (Pfeiffer Vacuum) and nXDS 10i dry scroll vacuum (Edwards Vacuum) pumps. A full range compact gauge (Pfeiffer Vacuum) was used to determine the pressure. Argon and nitrogen flows were controlled via mass-flow controllers (Teledyne Hastings Instruments). A HiPSTER 1 power supply unit (Ionautics) was used for initiating pulsed sputtering, and Aura-Wave ECR coaxial plasma sources (SAIREM) enabled generating the microwave volume plasma [24,25]. A rotary sample holder was attached to the chamber's lid, with the magnetron-substrate distance set to 12 cm. A GEN 1U 750 W power supply (TDK-Lambda) was connected to the substrate holder and the grounding was attached to the chamber's body. Further details can be found in [26].

2.2. Film fabrication

Thin films were fabricated via R-HiPIMS and MAR-HiPIMS. The sputtering target was a ∅ 50 mm, 3 mm thick, 99.999 % purity indium disc (Kurt J. Lesker Company). The substrates were ∅ 50 mm, 279 × 20 μm thick, n-type ⟨100⟩-oriented silicon wafers (MicroChemicals) and 76 × 26 × 1 mm glass slides (Carl Roth GmbH + Co. KG). The system was evacuated until reaching a minimum base pressure of 5×10^{-4} Pa. A pre-treatment step was applied for 5 min to remove organic pollutants and native oxides from the substrate's surface by exposing it to a microwave argon (UHP grade) plasma to induce so-called sputter cleaning. The parameters were as followed: 3 × 50 W MW power, 10 sccm of Ar, pressure of 0.2 Pa, and a DC substrate bias of −150 V. The deposition process was initiated directly after pre-treatment without breaking vacuum. With the MWs kept on to prevent contaminant redeposition onto the substrate, the In target was pre-sputtered underneath a shutter to remove any contaminants or oxides from its surface. The DC substrate bias was reduced to −20 V. Afterwards, the shutter was lifted and for R-HiPIMS the MW plasma was turned off. For MAR-HiPIMS, the microwave generators remained on for the duration of the process. Each process lasted 90 min to reach a film thickness of 100 nm, with the wafer fully rotating at 15 rpm to facilitate uniform deposition. The temperatures near the substrate, measured using a ∅ 1 mm, 50 mm microwave plasma-resistant temperature probe (Mesurex), were approx. 30 °C and 100 °C for the R- and MAR-HiPIMS processes, respectively.

2.3. Deposition environment analysis

The HiPISTER voltage-current outputs were monitored using a mixed signal oscilloscope (Tektronix). Data were acquired in averaging mode, based on 128 pulses.

Optical emission spectroscopy (OES) was performed using wavelength calibrated HR2000+ and HR2000CG-UV-NIR spectrometers (Ocean Optics), with spectral ranges of 200–480 nm and 200–1100 nm, respectively. The emitted light was transmitted from a 25 mm focal length f/2.8 quartz lens (Pentax) to the spectrometer using a QP400-2-SR-BX 200–1100 nm wavelength-ranged optical fibre (Ocean Optics).

Plasma properties near the substrate were obtained via Langmuir single probe (Impedans) measurements under sputtering and microwave plasma conditions. A voltage sweep from −20 to 30 V, with a step of 0.5 V, was applied to the ∅ 0.4 mm, 10 mm long tip and the resulting current was tracked. Microwave plasma characterisation was completed in time-averaged mode, whereas MAR-HiPIMS in time-resolved mode using a HiPSTER Sync Unit (Ionautics) as the external trigger.

The plasma's chemistry was determined using a prototype time-of-flight mass spectrometer (TOFWERK), providing mass spectra of all mass-to-charge ratios up to 500 Th with mass resolution (full width at half maximum, FWHM) of 500 for low mass-to-charge ratios (Ar^{2+}) and 1000 for heavier ions ($^{180}Hf^{+}$). The instrument includes an electrostatic energy analyser to measure plasma ion energies. A 20 μm orifice positioned at the substrate height was used to sample ions from the plasma into the mass spectrometer (via differentially pumped transfer optics). During measurements, the orifice plate was grounded and the residual pressure in the sampling ion optics was below 5×10^{-3} Pa. It was therefore assumed that collisions after the sampling orifice, potentially leading to charge transfer or recombination reactions, could be neglected.

2.4. Film analysis

X-ray diffraction (XRD) was performed via a PanAlytical Empyrean diffractometer (Malvern Panalytical), equipped with optics for primary and diffracted beam conditioning, and a 5-axis cradle as a sample holder. The exploited wavelength was Cu Kα = 1.5418 Å. Radial (θ/2θ) measurements were collected in the 2θ angular range from 20° to 90° in grazing incidence (GIXRD), with the incident angle fixed at 0.5°. The angular acceptance to the samples and detector were reduced via divergence and soller slits, as well as a parallel plate collimator for the detector. The angular resolution of the exploited setup was experimentally determined by measuring the FWHM of the rocking curve of the c-Si 004 reflection, which was 0.03°. Consequently, the presented measurements are considered to be within an accuracy interval of ±0.03°. The texture was analysed by performing a pole figure of the reflection of interest. The footprint of the X-ray beam on the sample's surface was

minimised to avoid drastic changes of irradiated volume during pole figure recording. Background modelling and subtraction, peak identification and fitting and phases identification were performed using the HighScore Plus software (Malvern Panalytical) [27]. All measured diffractograms resulted in a reliable fitting against pseudo Voigt functions. Texture analyses was completed using the X'Pert Texture software (Malvern Panalytical).

X-ray reflectometry (XRR) was performed using a D8 Discover X-Ray Diffractometer (Bruker) to estimate the films' density. The incident beam (Cu Kα = 1.5418 Å) was conditioned using a Göbel mirror. The measurements were done in a θ/2θ geometry, and the reflectivity diffractograms were analysed by fitting the data to a physical model. The model was created using the DIFFRAC LEPTOS 7 software (Bruker), by selecting a silicon base and a SiO_2 interlayer, with either In or InN as the top layer (density uncertainty determined to be approx. 5 %).

The fracture cross-sections and surface morphologies of the films were imaged using a Hitachi S-4800 high-resolution cold field emission scanning electron microscope (SEM) (Hitachi High-Tech Corporation). Transmission electron microscopy (TEM) was performed using a FEI Titan Themis 200 G3 (ThermoFisher) at 200 keV to characterise the structure and grain size of a 30 nm InN film deposited directly onto a TEM grid (copper grid + carbon membrane, Ted Pella). The integrated SuperX detector was used for energy dispersive X-ray spectroscopy (EDX).

The optical bandgap (E_{04}) of the films was characterised using an UVISEL spectroscopic ellipsometer (Horiba), with Drude and Tauc-Lorentz single oscillators to model the layers, and via a Lambda 950 UV/Vis/NIR spectrometer (PerkinElmer). Multi-model analysis was performed by combining the ellipsometry measurements with the total reflectance and transmittance of the spectrometer. The material's electron mobility was measured via an Ecopia HMS-3000 Hall Measurement System (Bridge Technology).

3. Results

3.1. HiPIMS pulse and plasma property analysis

During all experiments and depositions, the following parameters were used: 25 μs pulse width and 100 Hz repetition rate, with the HiPSTER operated in voltage-limited mode at −950 V, 0.6 Pa pressure and 60 sccm Ar flow. The nitrogen flow was varied from 0 to 40 sccm, as was the microwave power, ranging from 0 to 200 W on each of the three sources.

Firstly, the evolution of the HiPIMS discharge current as a function of nitrogen flow and MW power was investigated, with selected results shown in Fig. 1. For a pure Ar discharge, a peak current of 7 A is reached by the end of the 25 μs pulse. No significant influence of MW power on the characteristic current evolution was observed. When adding 20 sccm of nitrogen, a discharge time lag appears, meaning that a current is not detected for the first few microseconds. A delay in current onset is also present for 40 sccm N_2, with an additional change in discharge nature visible by the slower current rise. Upon turning on the MW plasma at 3 × 5 W, the time lag slightly increases. With continued sputtering, with or without the low MW power, the current onset delay is susceptible to variations. However, by increasing the MW power to 3 × 10 W, the time lag disappeared. Further increases in MW power do not seem to change the nature of the discharge for 20 sccm N_2. For the highest N_2 flow of 40 sccm, the increase in MW power induces the discharge current to rise at a significantly higher rate to reach a peak value just below 8 A.

Simultaneously, OES was performed facing the magnetron discharge to identify the type of generated species and track changes influenced by the N_2 flow and MW power. Example spectra (Fig. 2A,B) obtained under MAR-HiPIMS conditions show the emission of atomic In(I) and ionic In (II) [28], nitrogen's first positive system (FPS), second positive system (SPS), and first negative system (FNS), as well as the presence of atomic N [29,30] (selected emission lines listed in Table S1). Fig. 2C shows the changes in the In(I)/In(II) and atomic nitrogen/nitrogen species sum ratios as a function of N_2 flow and MW power. The MW plasma did not significantly influence In species generation, however, with increasing N_2 flow, the emission of In(II) dropped by around 10 % at 10, 20 and 30 sccm N_2, and 35 % at 40 sccm N_2. In contrast, the presence of MW plasma considerably affected the generation of various nitrogen species, most notably doubling the atomic N contribution at 3 × 200 W, with respect to the value obtained without MW plasma.

Langmuir probe measurements were performed under microwave plasma conditions for different N_2 flows and MW powers (Fig. 3A-C) to monitor their effect on the: plasma potential (V_p), electron temperature (kT_e), electron (N_e) and ion (N_i) densities. The V_p differed for pure Ar plasma and all Ar/N_2 plasmas, independently of the N_2 flow. The V_p for pure Ar plasma increases sharply with increasing MW power until reaching 15 V at 3 × 50 W, after which it does not greatly increase and stabilises at 18 V in the MW power range 3 × 100–200 W. The addition of N_2 causes a decrease in V_p, where at 3 × 50 W it is 12 V. However, for nitrogen-containing plasma, with increasing MW power, the V_p increases rapidly, until stabilising in the range of 3 × 100–200 W at 22 V. The kT_e is strongly influenced by the addition of N_2 to the discharge gas. The highest values were recorded for pure Ar plasma, where it reached a maximum value of 2.4 eV at 3 × 50 W. The kT_e significantly drops with the addition of N_2, with the maxima of approx. 1.7, 1.3, 1.1 and 1.0 eV for 10, 20, 30 and 40 sccm, respectively, reached at 3 × 75 W and stabilised around these values with increasing powers. The N_e and N_i did not differ significantly with the addition of N_2 and followed a similar trajectory with increasing MW power as the pure Ar plasma.

Next, time-resolved Langmuir probe measurements under MAR-HiPIMS conditions in the substrate region were performed to determine the effects of the HiPIMS and MW plasmas on one another (Fig. 3D-

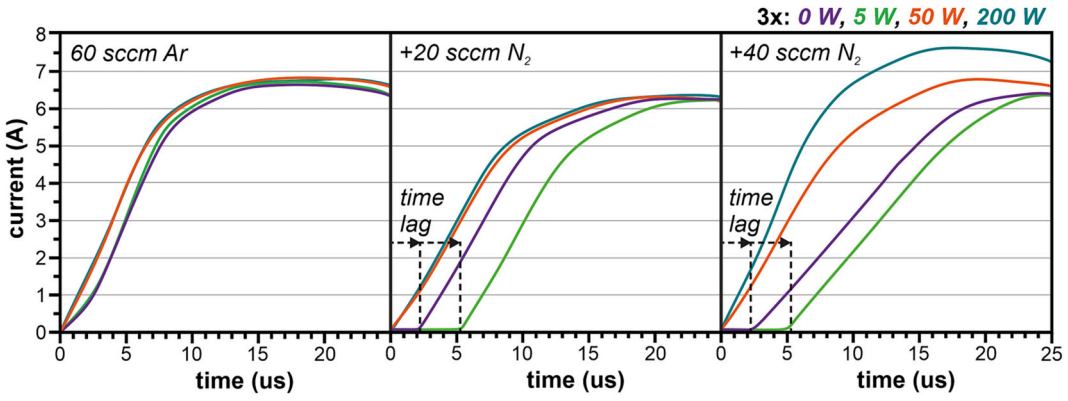

Fig. 1. Current evolution during In HiPIMS under varying MW plasma powers 3 × 0–200 W (3 MW sources) and Ar/N_2 flows: pure Ar flow, 60/20, and 60/40, sputtering conditions: 25 μs pulse width, 100 Hz sputtering frequency, −950 V discharge voltage, 0.6 Pa pressure.

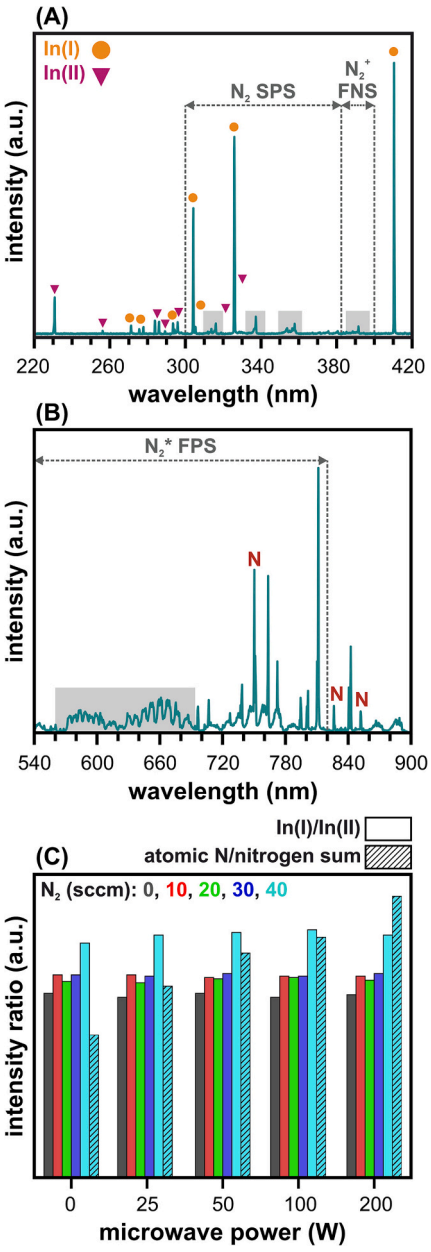

Fig. 2. (A, B) Example OES spectra obtained during MAR-HiPIMS (In HiPIMS: 25 µs, 100 Hz; MW: 60/40 sccm Ar/N_2, 3 × 200 W, 0.6 Pa), (C) changes in In (I)/In(II) ratios (full bars) and atomic N/N species sum ratio (lined), as a function of N_2 flow and MW power.

F). The HiPIMS pulse was initiated 20 µs after the Langmuir probe, at which point the initially measured plasma properties of the MW plasma change, resembling those of the HiPIMS plasma, with the V_p decreasing from 13 V to 5 V and the kT_e increasing from 1 eV to 3.5 eV. The drops in ion and electron density at the substrate height during the HiPIMS pulse and subsequent increase after the pulse are due to the charged species being drawn towards the magnetron via the high generated electric field.

Time-resolved ToF-MS (Fig. 4) allowed to simultaneously identify Ar^+, Ar^{2+}, N_2^+, N^+ and In^+ species in the substrate region. More importantly, however, the measurements enabled determining the energies of the incoming ions, which could be grouped into three energy/charge (E/Q) categories: *low* (0–6 V), *mid* (6–12 V), and *high* (12–20 V). The *low* and *high* E/Q groups were determined to originate from HiPIMS, with the increase in the number of ions detected within the timescale of

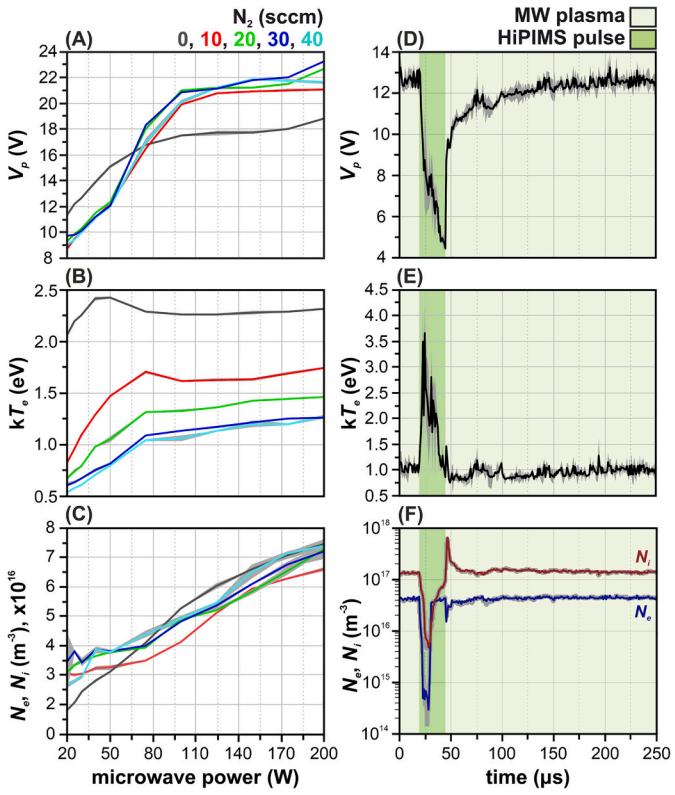

Fig. 3. Langmuir probe measurements of V_p, kT_e, N_e, and N_i at the substrate region (A-C) under MW plasma conditions for different N_2 flows and MW powers, (D—F) under MAR-HiPIMS sputtering conditions (In HiPIMS: 25 µs, 100 Hz; MW: 60/40 sccm Ar/N_2, 3 × 50 W, 0.6 Pa), grey areas mark measurement uncertainties, dark green areas mark pulse duration, pale green areas mark the period when only the MW plasma is on, scales adapted to the data range.

the HiPIMS 25 µs pulse, after which their population decreased. The *mid* E/Q ion group was associated with the MW plasma. During the HiPIMS pulse, the population of argon and nitrogen ions drops significantly, after which it quickly increases to its initial value. The upper E/Q of 12 V resembles the MW plasma's V_p (13 V). Furthermore, an increase in In^+ population is observed over the course of 75 µs after the HiPIMS pulse. Afterwards, the number of In^+ slowly decays at an exponential decay time of $\tau \approx 1.3$ ms.

3.2. InN film characterisation

Firstly, GIXRD was performed on films fabricated via R-HiPIMS and MAR-HiPIMS (Fig. 5A). For the R-HiPIMS samples, multiple peaks were registered, all assigned to metallic indium. The diffractogram of the MAR-HiPIMS sample contains only one peak, identified as (0002) oriented indium nitride (the other being from the Si substrate). A pole figure of the MAR-HiPIMS sample was prepared, with the (0002) pole in the centre (Fig. 5B), where fibre-texturing was determined with a high degree of mosaicity (intensity of the scattering extending over a Ψ range of approx. 15°). The density of the MAR-HiPIMS film measured via XRR was approx. 6.9 g/cm^3 (InN bulk density 6.9 g/cm^3 [31]), whereas the R-HiPIMS film density was greater at 7.1 g/cm^3 (In bulk density 7.3 g/cm^3).

SEM and TEM were used to characterise the films' microstructure and morphology (Fig. 6). The R-HiPIMS sample is characterised by high surface roughness and thickness inhomogeneities ranging from around 50 to 80 nm. Cauliflower-shaped grains, along with randomly distributed larger grains, are present on the film's surface. The MAR-HiPIMS film, in contrast, has a homogeneous thickness of 100 nm. The

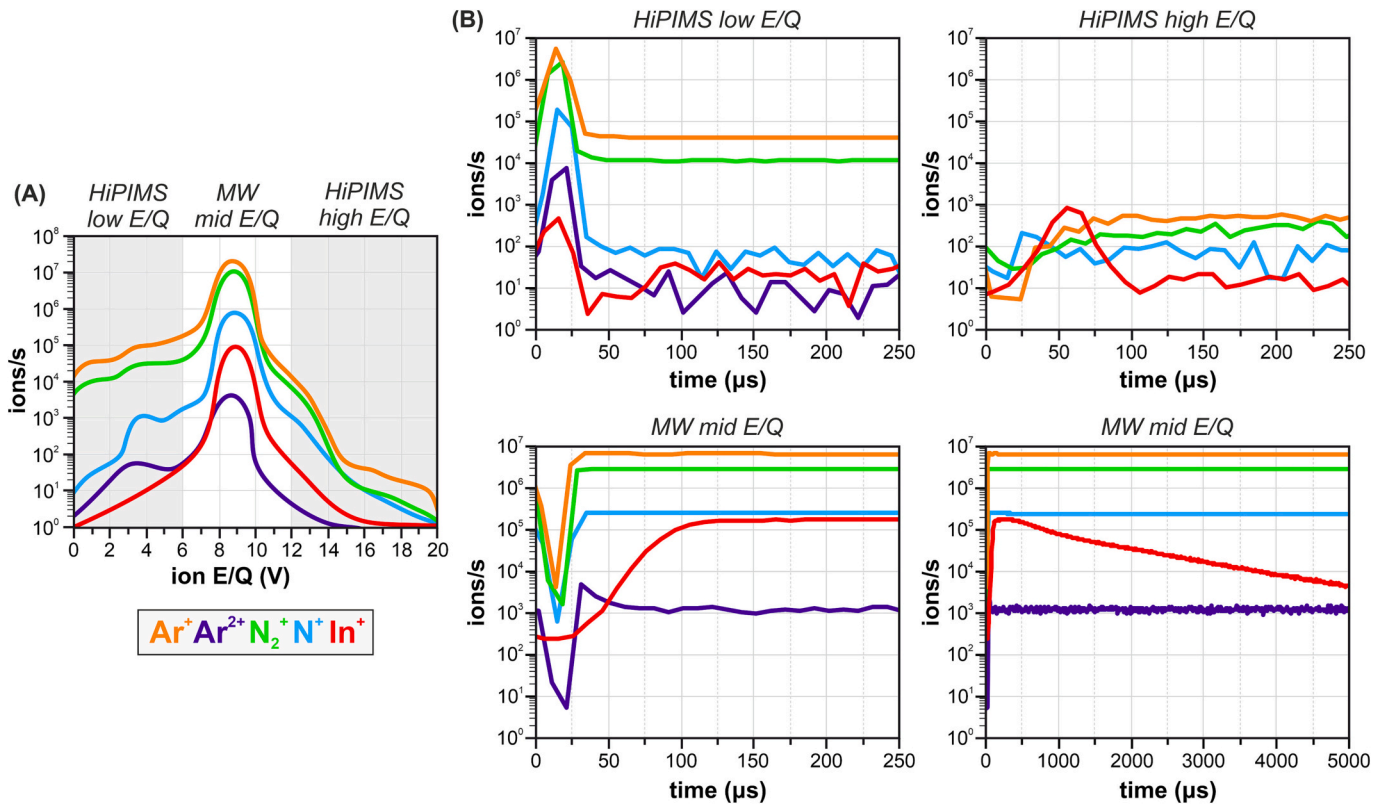

Fig. 4. ToF-MS measurements performed at the substrate region under MAR-HiPIMS sputtering conditions (In HiPIMS: 25 µs, 100 Hz; MW: 60/40 sccm Ar/N_2, 3 × 50 W, 0.6 Pa), (A) averaged ion E/Q distribution over entire measurement period, temporal evolution of: *low* and *high* E/Q groups (top), *mid* E/Q group (bottom).

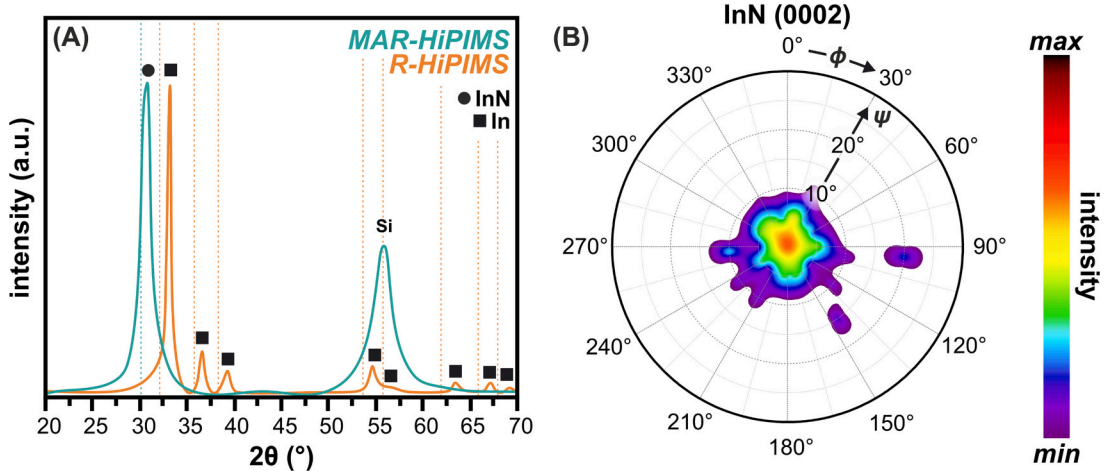

Fig. 5. (A) GIXRD of InN films deposited via R- and MAR-HiPIMS, dotted lines mark In and InN non-stressed positions [43] (B) pole figure of the MAR-HiPIMS sample with the InN (0002) pole in the centre.

fracture surface revealed columns, the tops of which are reflected in the extremely fine round features on the sample's surface (⌀ approx. 5 nm). The bright-field TEM (BF-TEM) images of the two samples show a continuous crystalline film for both cases. Selected area electron diffraction (SAED) confirms that without microwaves there is no nitride formation, with metallic indium being deposited instead. The microwave plasma-assisted process leads to a single phase of indium nitride with a <0001> out of plane texture (Fig. S1).

The local chemical composition was analysed using EDX mappings (Fig. S2). In the case of R-HiPIMS, only traces of nitrogen were found. Instead, a strong oxygen signal was present, which indicates the presence of a native oxide layer on the metallic indium grains. The MAR-HiPIMS film showed a roughly equal atomic percentages of nitrogen and indium corresponding to a stoichiometric InN phase. Its structure was studied in more detail using high-resolution scanning transmission electron microscopy (HR-STEM), as shown in Fig. 7. The grain size of

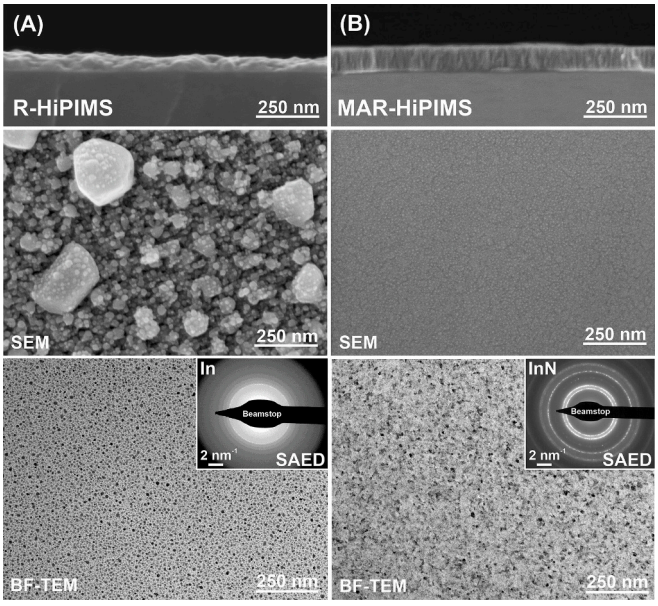

Fig. 6. SEM fracture cross-section and surface morphology (~100 nm film on Si substrates), TEM-BF imaging (~30 nm film on TEM grids) and SAED of films deposited via (A) R-HiPIMS and (B) MAR-HiPIMS.

InN lies in the range of 6–10 nm with most grains oriented close to a <0001> zone axis. In high resolution, InN's hexagonal structure is clearly visible (Fig. 7B), indicating a high degree of ordering within the grains.

Ellipsometry and UV/Vis/NIR spectroscopy were used to determine the films' optical properties. The results between the model and the spectroscopic measurements agree within the uncertainty limits. The results of the R-HiPIMS sample resembled those of a metal (in agreement with only In being detected), therefore it was not analysed further. For the MAR-HiPIMS sample, the E_{04} value from UV/Vis and ellipsometry were 1.56 and 1.50 eV, respectively (Fig. 8). Hall effect measurements were performed on the MAR-HiPIMS sample to determine its electron concentration and mobility, which were 2.72 × 10^{20} cm^{-3} and 7.16 cm^2V^{-1} s^{-1}, respectively.

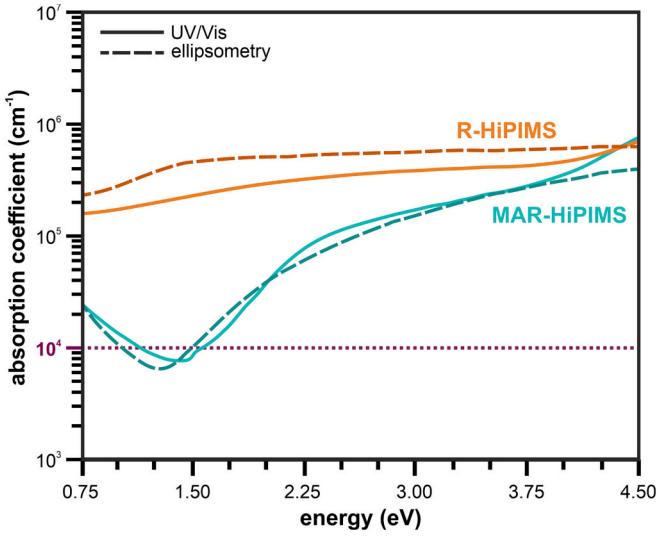

Fig. 8. Absorption coefficient vs energy obtained from UV–Vis (full line) and ellipsometry (dashed line) for R- and MAR-HiPIMS InN samples, dotted line marks the E_{04}.

4. Discussion

4.1. Deposition environment

During R-HiPIMS, the nitrogen introduced into the chamber is subjected to partial dissociation within the magnetron plasma during sputtering and reacts with the surface of the indium target to generate a compound layer. The properties of this layer will significantly differ from those of pure In and will, in turn, change the target's discharge dynamics [2,4,5,16,32]. One of the main aspects affected by indium nitriding is γ_{see}. It has been shown that under DCMS Ar^+ bombardment, In's γ_{see} upon nitriding and is almost halved [4], meaning that there will be fewer generated secondary electrons (SEs). This causes a discharge time lag, signalling that the initiation of HiPIMS discharges is hindered. Yushkov and Anders explain that this phenomenon is comprised of two components, i.e. a statistical time lag t_s, which is the time required for the initial electrons to appear in the electric field, and a formative time lag t_f, the time needed for developing the discharge from the initial

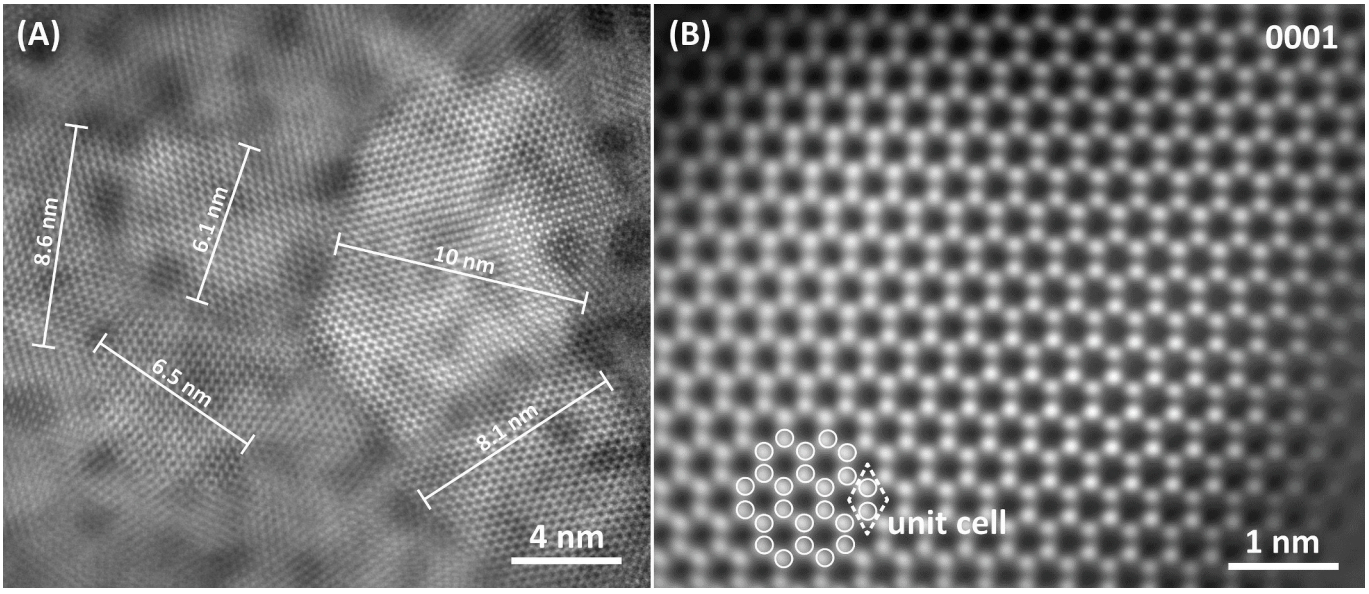

Fig. 7. HR-STEM images of MAR-HiPIMS InN film; (A) overview, showing the grain size and (B) close-up, showing the atomic structure of (0001) orientated InN.

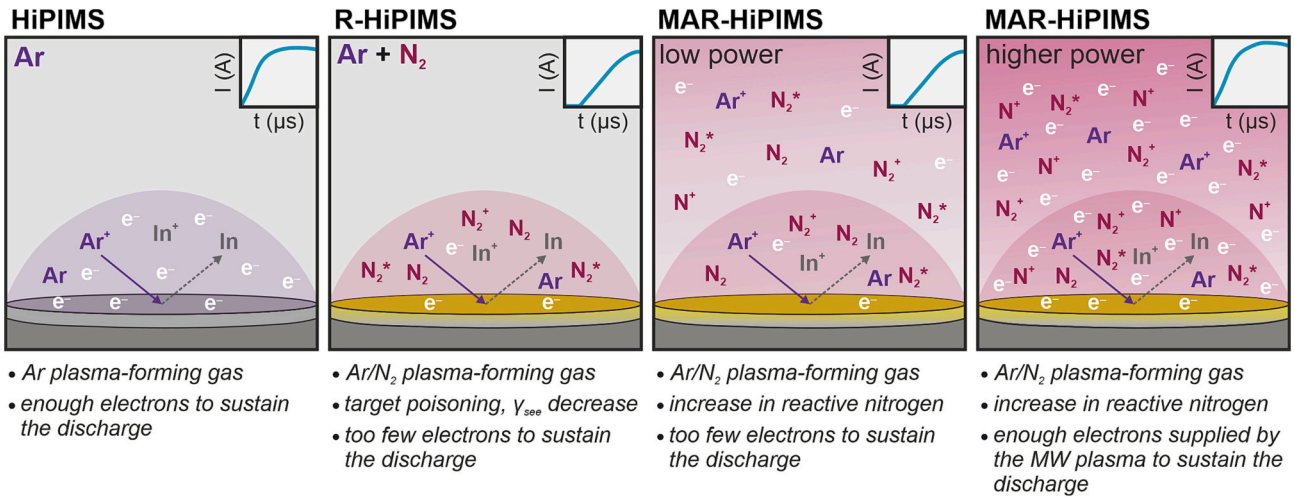

Fig. 9. Schematic representation of nitrogen reactivity vs electron generation during In sputtering via HiPIMS, R-HiPIMS, low and higher MW power MAR-HiPIMS.

electrons [5]. With an insufficient number of generated electrons to compensate the loss of charged particles due to the ion current, the discharge current is limited. Once there are enough electrons, the discharge proceeds as normal. It is possible to overcome this limitation to a certain extent by extending the HiPIMS pulse width, however, this is not a long-term solution. Another solution could be increasing the voltage, possibly allowing to reach greater currents and bypass the time lag (this was not explored in the scope of this work, as the used generators were limited to 1 kV). The negative effect of target poisoning may progress throughout the process's duration, continuously changing the discharge behaviour, in turn affecting the microstructure and properties of the fabricated film. With continued target poisoning, the time lag can increase, compromising discharge ignition.

Filling the chamber with a volume MW plasma in a pure Ar discharge does not induce significant changes (Fig. 1A). However, a notable effect is observed once nitrogen is added (Figs. 1B,C, 2). For low MW powers (here, below 3 × 10 W), a greater quantity of reactive nitrogen is created, causing more reactions on the In target's surface, increasing the time lag. Further MW power increases, however, not only activate more reactive nitrogen species, but additionally increase ion and electron densities within the chamber, providing electrons to the magnetron discharge. Now there are enough seed electrons to overcome the negative effect of γ_{see} decrease, causing the time lag to disappear. Therefore, it can be summarised that the advantage of including microwave plasma during R-HiPIMS is twofold, *(1)* activating the otherwise inert nitrogen molecules to ensure attaining stoichiometric InN films, and *(2)* suppling seed electrons near the magnetron to compensate for the decrease in SEs caused by compound layer formation (Fig. 9).

Gas discharge plasma in Ar/N_2 mixtures is rather well understood [33–35]. However, which of the possible reactions and reaction pathways, including electron impact ionisation, dissociative ionisation, vibrational excitation, and vibrational pumping, to name only few, are dominant depends strongly on the total gas pressure, mixture and excitation mechanisms. Langmuir probe measurements (Fig. 3) show a decrease in kT_e upon N_2 addition, which is caused by the vibrational excitation of N_2 via collisions with plasma electrons. Similar effects were observed by Zhiguo et al. within an Ar/N_2 MW-ECR plasma [10]. Furthermore, the reported MW plasma densities are in the same order of magnitude as those reported by Zoubian et al. using the same MW-ECR sources [36], for the given distance between the MW source and Langmuir probe tip, with the trends following higher densities with greater MW powers.

When igniting the HiPIMS discharge under MW plasma conditions, Langmuir probe results depicted similar trends reported and explained by Hain et al. [26] and Stranak et al. [37]. Considerable perturbations are introduced to the MW plasma, where the negative electric field (−950 V) draws the ions from the substrate region towards the magnetrons causing the observed plasma property changes to those typical for HiPIMS. Further displacement currents are observed at the end of the HiPIMS discharge, i.e. lack of electric field, reflected by the N_e and N_i values just after the pulse. Moreover, an increase in N_i is observed, which would correspond to ions reaching the substrate once released from the magnetron trap.

The ToF-MS results complement Langmuir probe observations, as well as enable determining which of the detected species are generated by the HiPIMS discharges and which by the MW plasma. As mentioned in the Results section, it was possible to distinguish three E/Q ranges (Fig. 4). The *low* and *high* ranges were attributed to the HiPIMS discharge, where the time profiles show an increase in In ions near the end and after the end of the pulse. Within the *low* range, an increase in argon and nitrogen species is observed. As N^+ is detected, it can be stated that a certain amount of nitrogen is dissociated within the magnetron plasma, with the ratio between molecular and atomic species detected during the pulse being approx. 40. The *mid* E/Q ion group was determined to be generated within the MW plasma, where the number of measured argon and nitrogen ions is stable over the entire measurement period, except in the time frame of the magnetron pulse. During that time, a drop in measured species is observed, which corresponds to the behaviour of the plasma potential measured via the Langmuir probe. Following OES results, where an increase in nitrogen peak intensities were detected in the presence of MW (Fig. 2), the ratio between molecular and atomic nitrogen is approx. 12. Therefore, the MW plasma facilitates nitrogen dissociation, and does so much more effectively than the HiPIMS plasma. In terms of In ion behaviour, long decay times were registered during both R-HiPIMS (results not included) and MAR-HiPIMS, which is consistent with long term decay rates of heavy sputtered species in the HiPIMS afterglow [38]. However, in the presence of MW plasma, the amount of detected In^+ over the entire measurement cycle increased by 185 %. The results indicate that the microwave plasma facilitates the transfer of charged particles from the dense plasma generated during In HiPIMS towards the substrate, while inducing post-sputtering ionisation.

4.2. InN film characteristics vs fabrication conditions

To determine the influence of the deposition environment on the structuring and properties of InN films, R-HiPIMS and MAR-HiPIMS samples were prepared. Directly, it could be determined that without MW plasma it was not possible to produce InN. Both X-ray and electron diffraction identified the material deposited using R-HiPIMS to be

metallic indium. As the R-HiPIMS sample was mainly metallic, focus was placed on the MAR-HiPIMS film. GIXRD showed that InN was obtained, preferentially growing in the (0002) direction. From the pole figure it was possible to determine a fibre-type texture, with a high level of grain mosaicity. This was confirmed via TEM investigations, where the InN grains were predominantly oriented close to a $< 0001 >$ zone axis, with visible z-axis rotation of the grains, in respect to one another.

The optical band gap of the MAR-HiPIMS film (approx. 1.5 eV) is in range of values reported for polycrystalline InN. The measured electron concentration (2.72×10^{20} cm^{-3}) and mobility (7.16 cm^2V^{-1} s^{-1}) are also characteristic for films deposited via sputtering [6,39]. For reported values of perfect InN films, deposited, e.g. by molecular beam epitaxy (MBE), with electron concentrations in the range of 10^{17} cm^{-3}, the electron mobility can exceed 3000 cm^2V^{-1} s^{-1} [40,41]. In the work of Walukiewicz *et. al* [42], an absorption edge of 1.5 eV (or a Burstein-Moss shift of 0.8 eV) induced by an electron concentration of $n = 2 \times 10^{20}$ cm^{-3} was reported. The strength of this Burstein-Moss shift is due to the Fermi stabilisation energy (E_{FS}) penetrating the conduction band of InN. Intrinsic defects will then tend to be n-type, which will make the fermi level (E_F) rise until reaching E_{FS}. Although imperfect, the InN layer fabricated via MAR-HiPIMS matches the characteristics described in literature for defective InN. A possible reason behind the low electron mobility and high electron concentration may be explained by the high degree of grain mosaicity. In these locations, dangling bonds can remain non-passivated, which would flood the layer with surplus electrons, and function as defects/traps for electron recombination. Further studies into improving the applicational properties of InN should include controlling the energy of incoming species. As MAR-HiPIMS facilitates ion generation, it would be possible to steer their behaviour through the application of electric fields near the substrate, e.g. substrate biasing and/or MW plasma pulsing. This should enable reducing prolonged Ar ion bombardment, potentially leading to structure degradation and amorphisation [13,26].

5. Conclusions

This work focused on characterising the deposition environment and fabricated thin films via MAR-HiPIMS, where an In target was sputtered in the presence of a mixed Ar/N_2 MW plasma. The combination of in situ diagnostics and material characterisation allowed to conclude the following:

- Indium is susceptible to target poisoning through surface reactions with nitrogen, with the formation of a compound layer causing a delay in current onset,
- Microwave plasma provides enough electrons to sustain the HiPIMS discharge and facilitates inert molecular nitrogen dissociation into reactive metastable molecular and atomic species,
- Coupling time-resolved Langmuir probe and ToF-MS measurements allow to characterise the behaviour of the HiPIMS and MW plasmas, by monitoring the temporal evolution of the plasma properties, determining the plasma chemistry, and identifying the origin of the detected ions based on their energies,
- MAR-HiPIMS is successful in fabricating stoichiometric textured InN films, with a high degree of grain mosaicity, with the material's optoelectronic properties within the range of sputtered InN.

Future studies should focus on controlling the incoming charged species, as this could be key in decreasing grain mosaicity, and modifying the optoelectronic properties of the InN film. Different possibilities present themselves, such as synchronising the HiPIMS pulse and the substrate bias and/or MW plasma pulsing to reduce the number of argon ions bombarding the surface of the growing film.

CRediT authorship contribution statement

C. Hain: conceptualisation, depositions, investigations and analysis, preparing original draft, graphics; *P. Schweizer*, *P. Sturm*, *A. Borzì*, *J. E. Thomet*: investigations and analysis, draft revision and editing; *J. Michler*, *A. Hessler-Wyser*, *T. Nelis*: supervision, resources, draft revision and editing; supervision, draft revision and editing;

Declaration of competing interest

The authors declare no known competing financial interests or personal relationships that could have influenced the work reported in this paper.

Data availability

Data will be made available on request.

Acknowledgements

This work was co-funded by the Innosuisse - Swiss Innovation Agency and the European Union as part of projects E!114277 IonDrive and E!12507 Plasma S^3Tream.

Appendix A. Supplementary data

Supplementary data to this article can be found online at https://doi.org/10.1016/j.surfcoat.2022.129188.

References

[1] D. Depla, S. Mahieu, Reactive Sputter Deposition, Springer Berlin Heidelberg, Berlin, Heidelberg, 2008, https://doi.org/10.1007/978-3-540-76664-3.
[2] A. Anders, Tutorial: reactive high power impulse magnetron sputtering (R-HiPIMS), J. Appl. Phys. 121 (2017), https://doi.org/10.1063/1.4978350.
[3] D. Güttler, B. Abendroth, R. Grötzschel, W. Möller, D. Depla, Mechanisms of target poisoning during magnetron sputtering as investigated by real-time in situ analysis and collisional computer simulation, Appl. Phys. Lett. 85 (2004) 6134–6136, https://doi.org/10.1063/1.1835002.
[4] D. Depla, S. Mahieu, R. de Gryse, Magnetron sputter deposition: linking discharge voltage with target properties, Thin Solid Films 517 (2009) 2825–2839, https://doi.org/10.1016/j.tsf.2008.11.108.
[5] G.Y. Yushkov, A. Anders, Origin of the delayed current onset in high-power impulse magnetron sputtering, IEEE Trans. Plasma Sci. (2010) 3028–3034, https://doi.org/10.1109/TPS.2010.2063041.
[6] B.R. Natarajan, A.H. Eltoukhy, J.E. Greene, T.L. Barr, Mechanisms of reactive sputtering of indium I: growth of InN in mixed ar-N2 discharges, Thin Solid Films 69 (1980) 201–216, https://doi.org/10.1016/0040-6090(80)90037-1.
[7] B.T. Sullivan, R.R. Parsons, K.L. Westra, M.J. Brett, Optical properties and microstructure of reactively sputtered indium nitride thin films, J. Appl. Phys. 64 (1988) 4144–4149, https://doi.org/10.1063/1.341326.
[8] T. Maruyama, T. Morishita, Indium nitride thin films prepared by radio-frequency reactive sputtering, J. Appl. Phys. 76 (1994) 5809–5812, https://doi.org/10.1063/1.358480.
[9] M. Amirhoseiny, Z. Hassan, S.S. Ng, M.A. Ahmad, Characterizations of InN thin films grown on Si (110) substrate by reactive sputtering, J. Nanomater. 2011 (2011), https://doi.org/10.1155/2011/579427.
[10] Z. Zhiguo, L. Tianwei, X. Jun, D. Xinlu, D. Chuang, N-rich zr-N films deposited by unbalanced magnetron sputtering enhanced with a highly reactive MW-ECR plasma, Surf. Coat. Technol. 200 (2006) 4918–4922, https://doi.org/10.1016/j.surfcoat.2005.04.060.
[11] W.A. Bryden, S.A. Ecelberger, T.J. Kistenmacher, Heteroepitaxial growth of InN on AlN-nucleated (00.1) sapphire by ultrahigh vacuum electron cyclotron resonance-assisted reactive magnetron sputtering, Appl. Phys. Lett. 64 (1994) 2864–2866, https://doi.org/10.1063/1.111451.
[12] C. Takahashi, M. Kiuchi, T. Ono, S. Matsuo, An electron cyclotron resonance plasma deposition technique employing magnetron mode sputtering, J. Vac. Sci. Technol. A 6 (1988) 2348–2352, https://doi.org/10.1116/1.575588.
[13] A. Raveh, M. Weiss, R. Schneck, Optical emission spectroscopy as a tool for designing and controlling the deposition of graded TiAlN layers by ECR-assisted reactive RF sputtering, Surf. Coat. Technol. 111 (1999) 263–268, https://doi.org/10.1016/S0257-8972(98)00823-8.
[14] V.Y. Davydov, A.A. Klochikhin, R.P. Seisyan, V.V. Emtsev, S.V. Ivanov, F. Bechstedt, J. Furthmüller, H. Harima, A.V. Mudryi, J. Aderhold, O. Semchinova, J. Graul, Absorption and emission of hexagonal InN. Evidence of narrow fundamental band gap, Phys. Status Solidi B Basic Res. 229 (2002) r1–r3, https://

doi.org/10.1002/1521-3951(200202)229:3%3CR1::AID-PSSB99991%3E3.0.CO;2-O.
[15] T.L. Tansley, C.P. Foley, Optical band gap of indium nitride, J. Appl. Phys. 59 (1986) 3241–3244, https://doi.org/10.1063/1.336906.
[16] A.G. Bhuiyan, A. Hashimoto, A. Yamamoto, Indium nitride (InN): a review on growth, characterization, and properties, J. Appl. Phys. 94 (2003) 2779–2808, https://doi.org/10.1063/1.1595135.
[17] T. Miyajima, Y. Kudo, K.-L. Liu, T. Uruga, T. Honma, Y. Saito, M. Hori, Y. Nanishi, T. Kobayashi, S. Hirata, Structure analysis of InN film using extended X-ray absorption fine structure method, Phys. Status Solidi B 234 (2002) 801–804, https://doi.org/10.1002/1521-3951(200212)234:3<801::AID-PSSB801>3.0.CO;2-W.
[18] V.W.L. Chin, T.L. Tansley, T. Osotchan, Electron mobilities in gallium, indium, and aluminum nitrides, J. Appl. Phys. 75 (1994) 7365–7372, https://doi.org/10.1063/1.356650.
[19] J.B. MacChesney, P.M. Bridenbaugh, P.B. O'Connor, Thermal stability of indium nitride at elevated temperatures and nitrogen pressures, Mater. Res. Bull. 5 (1970) 783–791, https://doi.org/10.1016/0025-5408(70)90028-0.
[20] I. Gorczyca, T. Suski, N.E. Christensen, A. Svane, Band gap bowings and anomalous pressure effects in III-V nitride alloys: role of in-segregation, Phys. Status Solidi A 208 (2011) 1558–1561, https://doi.org/10.1002/pssa.201000939.
[21] S.V. Ivanov, T.V. Shubina, T.A. Komissarova, V.N. Jmerik, Metastable nature of InN and In-rich InGaN alloys, J. Cryst. Growth (2014) 83–89, https://doi.org/10.1016/j.jcrysgro.2014.06.019. Elsevier.
[22] H. Itagaki, S. Hirose, J. Kim, M. Ogura, X. Wang, A. Nonaka, H. Ogiso, H. Sakakita, A low-power nitriding technique utilizing a microwave-excited radical flow, Jpn. J. Appl. Phys. 55 (2016) 06HC05, https://doi.org/10.7567/JJAP.55.06HC05.
[23] K.L. Westra, R.P.W. Lawson, M.J. Brett, The effects of oxygen contamination on the properties of reactively sputtered indium nitride films, J. Vac. Sci. Technol. A 6 (1988) 1730–1732, https://doi.org/10.1116/1.575280.
[24] L. Latrasse, M. Radoiu, T. Nelis, O. Antonin, Self-matching plasma sources using 2.45 GHz solid-state generators: microwave design and operating performance, J. Microw. Power Electromagn. Energy 51 (2017) 237–258, https://doi.org/10.1080/08327823.2017.1388338.
[25] L. Latrasse, A. Lacoste, J. Sirou, J. Pelletier, High density distributed microwave plasma sources in a matrix configuration: concept, design and performance, in: Plasma Sources Sci. Technol., IOP Publishing, 2007, pp. 7–12, https://doi.org/10.1088/0963-0252/16/1/002.
[26] C. Hain, D. Brown, A. Welsh, K. Wieczerzak, R. Weiss, J. Michler, A. Hessler-Wyser, T. Nelis, From pulsed-DCMS and HiPIMS to microwave plasma-assisted sputtering: their influence on the properties of diamond-like carbon films, Surf. Coat. Technol. (2021), 127928, https://doi.org/10.1016/j.surfcoat.2021.127928.
[27] T. Degen, M. Sadki, E. Bron, U. König, G. Nénert, The High Score Suite, in: Powder Diffr, Cambridge University Press, 2014, pp. S13–S18, https://doi.org/10.1017/S0885715614000840.
[28] NIST: Atomic Spectra Database Lines Form, (n.d.). https://physics.nist.gov/PhysRefData/ASD/lines_form.html (accessed February 21, 2022).
[29] S. Kosaraju, J.A. Marino, J.A. Harvey, C.A. Wolden, The role of argon in plasma-assisted deposition of indium nitride, J. Cryst. Growth 286 (2006) 400–406, https://doi.org/10.1016/j.jcrysgro.2005.10.069.
[30] M.A. Song, Y.W. Lee, T.H. Chung, Characterization of an inductively coupled nitrogen-argon plasma by langmuir probe combined with optical emission spectroscopy, Phys. Plasmas. 18 (2011), https://doi.org/10.1063/1.3554706.
[31] S. Krukowski, A. Witek, J. Adamczyk, J. Jun, M. Bockowski, I. Grzegory, B. Lucznik, G. Nowak, M. Wróblewski, A. Presz, S. Gierlotka, S. Stelmach, B. Palosz, S. Porowski, P. Zinn, Thermal properties of indium nitride, J. Phys. Chem. Solids 59 (1998) 289–295, https://doi.org/10.1016/S0022-3697(97)00222-9.
[32] A.A. Barybin, V.I. Shapovalov, Nonisothermal chemical model of reactive sputtering, J. Appl. Phys. 101 (2007), 054905, https://doi.org/10.1063/1.2435795.
[33] Y. Wang, J. Shi, C. Li, C. Feng, H. Ding, Comparative study of electron temperature in cascaded arc Ar/N2 plasma using laser Thomson scattering combined optical emission spectroscopy approach, AIP Adv. 9 (2019), 125307, https://doi.org/10.1063/1.5106401.
[34] N. Dyatko, Y. Ionikh, A. Napartovich, Influence of nitrogen admixture on plasma characteristics in a dc argon glow discharge and in afterglow, Atoms. 7 (2019) 13, https://doi.org/10.3390/atoms7010013.
[35] H. Muta, M. Koga, N. Itagaki, Y. Kawai, Numerical investigation of a low-electron-temperature ECR plasma in Ar/N2 mixtures, Surf. Coat. Technol. 171 (2003) 157–161, https://doi.org/10.1016/S0257-8972(03)00261-5.
[36] F. Zoubian, N. Renaut, L. Latrasse, Distributed elementary ECR microwave plasma sources supplied by solid state generators for production of large area plasmas without scale limitation: plasma density measurements and comparison with simulation, Plasma Res. Express. 3 (2021), 025010, https://doi.org/10.1088/2516-1067/ac0499.
[37] V. Stranak, A.P. Herrendorf, S. Drache, M. Cada, Z. Hubicka, R. Bogdanowicz, M. Tichy, R. Hippler, Plasma diagnostics of low pressure high power impulse magnetron sputtering assisted by electron cyclotron wave resonance plasma, J. Appl. Phys. 112 (2012), 093305, https://doi.org/10.1063/1.4764102.
[38] A. Hecimovic, A.P. Ehiasarian, Temporal evolution of the ion fluxes for various elements in HIPIMS plasma discharge, IEEE Trans. Plasma Sci. 39 (2011) 1154–1164, https://doi.org/10.1109/TPS.2011.2106516.
[39] W.A. Bryden, S.A. Ecelberger, T.J. Kistenmacher, Heteroepitaxial growth of InN on AlN-nucleated (00.1) sapphire by ultrahigh vacuum electron cyclotron resonance-assisted reactive magnetron sputtering, Appl. Phys. Lett. 64 (1994) 2864–2866, https://doi.org/10.1063/1.111451.
[40] T.B. Fehlberg, G.A. Umana-Membreno, B.D. Nener, G. Parish, C.S. Gallinat, G. Koblmüller, S. Rajan, S. Bernardis, J.S. Speck, Characterisation of multiple carrier transport in indium nitride grown by molecular beam epitaxy, Jpn. J. Appl. Phys. Lett. 45 (2006), L1090, https://doi.org/10.1143/JJAP.45.L1090.
[41] H. Liu, X. Wang, Z. Chen, X. Zheng, P. Wang, B. Sheng, T. Wang, X. Rong, M. Li, J. Zhang, X. Yang, F. Xu, W. Ge, B. Shen, High-electron-mobility InN epilayers grown on silicon substrate, Appl. Phys. Lett. 112 (2018), 162102, https://doi.org/10.1063/1.5017153.
[42] W. Walukiewicz, J.W. Ager, K.M. Yu, Z. Liliental-Weber, J. Wu, S.X. Li, R.E. Jones, J.D. Denlinger, Structure and electronic properties of InN and in-rich group III-nitride alloys, J. Phys. D. Appl. Phys. 39 (2006) R83, https://doi.org/10.1088/0022-3727/39/5/R01.
[43] A. Jain, S.P. Ong, G. Hautier, W. Chen, W.D. Richards, S. Dacek, S. Cholia, D. Gunter, D. Skinner, G. Ceder, K.A. Persson, Commentary: the materials project: a materials genome approach to accelerating materials innovation, APL Mater. 1 (2013), 011002, https://doi.org/10.1063/1.4812323.